Upwelling of Particulate Matter on Continental Slopes

J. Kämpf[1]

[1]College of Science and Engineering, Flinders University, Adelaide, Australia.

Corresponding author: Jochen Kaempf (jochen.kaempf@flinders.edu.au)

Key Points:

- Explores the dispersal of particles within steady-state stratified flows along continental slopes
- Shows that narrow submarine channels can facilitate a diapycnal up-channel flux of particles
- Particle upwelling continues to exist even with large particles settling speeds.

Abstract

Using the method of process-oriented hydrodynamic modelling, this work investigates the dispersal of particles, representing particulate organic matter in the ocean, within stratified fluids. The focus is placed on steady-state Eulerian density fields in which advective and diffusive processes are in balance. In such situations, particles are still advected across isopycnal surfaces, given that turbulent fluctuations do generally not offset the advective displacement of a particle. Here it is demonstrated that the interaction of currents with narrow submarine channels can facilitate a continuous diapycnal up-channel flux of particles. If the particles remain suspended in the water column, this upwelling even intensifies for negatively buoyant particles with settling speeds of up to 5 mm/s. Hence, this study uncovers a mechanism that (i) returns settling particles upward on continental slopes and that (ii) leads to a concentration of particulate matter in and around submarine channels. The author postulates that this physical concentration mechanism is central to marine food webs based on suspension feeding.

Plain Language Summary

Suspension feeders constitute a branch of marine food webs is based on consumption of particulate organic matter settling through the water column. This work demonstrates that the interaction of oceanic flows with submarine channels creates a situation in which particles of organic matter are channeled upward on the continental slope. This finding is the first concrete scientific evidence explaining why bathymetric undulations can trigger the creation of localized marine food webs via the concentration and accumulation of organic matter.

1 Introduction

The localized upwelling of seawater with elevated levels of dissolved nutrients is a principal trigger of highly productive marine food webs based on the creation of phytoplankton blooms in the euphotic zone (see Kämpf and Chapman, 2016). Due to the advances in satellite technology and modern marine instrumentation, physical mechanisms leading to surface phytoplankton blooms are well understood from the analyses of sea surface temperature, chlorophyll-*a* concentrations, and nutrient distributions. The associated marine-food webs may be classified as surface-driven food webs.

This work explores another, little understood type of marine food web that is driven by the spatial concentration of particulate organic matter and its attraction of suspension feeders (e.g., Hentschel and Shimeta, 2008). In contrast to surface-driven food webs, suspension feeding does not directly rely on the availability of sunlight. While it seems most likely that such marine food webs are initiated in the benthic zone near the seafloor, it has been suggested that mesoscale eddies can influence the particulate matter flux in the ocean interior (e.g. Siegel et al., 1990; Liu et al., 2018).

Benthic marine food webs become spatially concentrated for various reasons. For instance, hydrothermal vents in the deep sea support their own localized endemic marine ecosystems with hundreds of different species including crabs, shrimps, fish, and octopus as well as sessile creatures such as barnacles, limpets, feather stars, and tube worms (e.g. Mullineaux et al., 2018). Similarly, carbon seeps, often found in submarine canyons on the continental margin (e.g. Collier and Lilley, 2005), support the formation of diverse marine food webs including ample microorganisms, macrofaunal assemblages, macro-benthos and aggregations of crabs and lobsters (e.g. Levin et al., 2015).

The feeding behavior of whales is another indicator of possible nutrient concentrations at depth. Baleen whales do not only feed on plankton created in surface upwelling systems, but also on krill, that – as suspension feeders – are often found in the upper reaches of submarine canyons on the upper continental slope (e.g. Santora et al., 2018). The physical mechanisms that operate to concentrate particulate organic matter in or around submarine canyons are not well understood.

The behavior of particles within fluids has been studied over centuries from the early and famous particle settling studies by Stokes (1851), theories on relative viscosities of particle suspensions by Einstein (1906) or the dispersion by single particles (Taylor, 1922). In oceanographic studies, satellite-tracked surface drifters were used to analyze horizontal flow trajectories and to calculate effective turbulent diffusivities. Using hydrodynamic models, virtual Lagrangian particles are commonly used to infer the dispersal of marine species in their larval stage in studies of marine connectivity (e.g. Kämpf et al., 2010). Particles are also used to determine the theoretical age of water parcels (e.g. Delhez et al., 1999; Sandery and Kämpf, 2007). See van Sebil et al. (2018) for a comprehensively discussion of the fundamentals and practices of the physical-based Lagrangian ocean analysis. Ådlandsvik et al. (2009) give an overview of Lagrangian modelling practice from a marine biology perspective. Using the method of process-oriented modelling, here particles are used to study their potential upwelling pathways on continental slopes in the presence of density stratification.

2 Materials and Methods

2.1 Conceptual model

This work is based on the fundamental feature that particles can move relative to the ambient density field. In a steady-state density field, for instance, advective effects due to currents are balanced by diffusive effects due to turbulence. However, the same currents that no longer modify the density field can move an individual particle across isopycnal surfaces, given that turbulent fluctuations only modify but not offset particle movements. One prominent example of such persistent diapycnal movement of particles is the trapping of suspended sediment within high-turbidity regions in positive estuaries (e.g. Yu et al., 2015). In the same sense, the author postulates the existence of upwelling currents at continental margins that, while maintaining a steady-state density field, trigger the continuous upslope flow of particles (**Figure 1**).

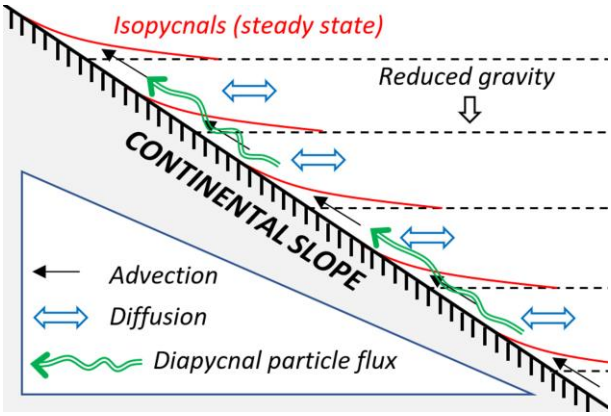

Figure 1: Schematic representation of particle fluxes across isopycnal surfaces of an ambient steady-state density field on a continental slope. Arrows indicate the velocity field.

2.2 Description of hydrodynamic model

This study applies the hydrodynamic shelf model called COHERENS (Coupled Hydrodynamical-Ecological Model for REgioNal Shelf Seas) (Luyten et al., 1999). The governing equations are the finite-difference forms of conservation equations for momentum, heat, volume and scalars (salinity) for an incompressible fluid on the *f* plane cast in terrain-following sigma coordinates. For more details, see Luyten et al. (1999). The Coriolis parameter is arbitrarily chosen at $f = -1\times10^{-4}$ s^{-1}, corresponding to a geographical latitude of 45°S. Findings can be readily adopted for the northern hemisphere. In this process-oriented application, temperature effects are ignored. The density of seawater, ρ, is related to salinity, S, via a linear equation of state:

$$\rho(S) = \rho_o[1 + \beta(S - S_o)] \quad (1)$$

where ρ_o = 1026 kg/m^3, $\beta = 7.6\times10^{-4}$ and S_o = 34 (no units). Vertical diffusion of momentum and density is parameterized by means of a k-ε turbulence closure scheme adopting standard parameter settings. A quadratic bottom-friction parameterization is employed using a bottom roughness length of 2 mm. Horizontal eddy viscosity is formulated by the Smagorinsky formula

using a value of 0.4 for the free parameter (see Oey et al., 1985). Variations of turbulence and friction parameters within reasonable ranges yielded similar results.

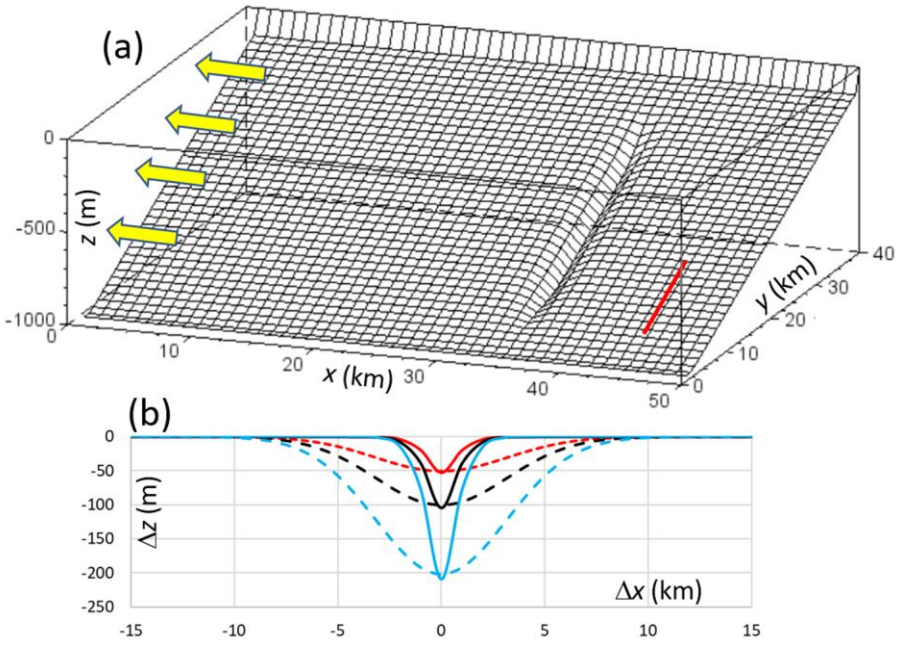

Figure 2: a) Model bathymetry. The arrows indicate the direction of the ambient geostrophic flow. The red line indicates the deployment region of Lagrangian floats. b) Different submarine channel/canyon geometries considered in a range of experiments (see Table 1).

In the original model formulation, the buoyancy force is calculated with reference to the initial density distribution. This can trigger the creation of unwanted currents due to the initial coordinate adjustment of the density field. In this application, horizontal gradients of the buoyancy force are calculated with reference to their initial values (of horizontal gradients). This technique eliminates such adjustment problems.

COHERENS contains a sophisticated Lagrangian particle module in which the gridded velocity field is projected onto the particle's location and particle movements are calculated from accurate logarithmic displacement laws (Luyten et al., 1999). This module includes turbulent displacements. Following Maier-Reimer (1980) the associated maximum turbulent velocity components can be calculated from:

$$(u^T_{\max}, v^T_{\max}, w^T_{\max}) = \sqrt{6(D_h, D_h, D_z)/\Delta t} \qquad (2)$$

where D_h and D_z are horizontal and vertical diffusivities and Δt is the numerical time step. The turbulent velocities are then determined for each particle with the Monte-Carlo method which consists in multiplying each maximum current component by a random generated number between -1 and 1. These diffusive velocity components are then added to the advective velocity components before the calculation of particle displacements.

Table 1: Configuration of experiments with numbers of upwelled and trapped particles

Experiment	10^{-3} N (s^{-1})	W (km)	H (m)	Ro[1]	Fr[1]	Bu	Σupwelled[3]	Σtrapped[3]
A-narrow	2.71	3	50	0.7	1.5	0.21	72	6
A-narrow-w	*0.86*	*3*	*50*	*0.7*	*4.7*	*0.02*	*1*	*0*
A-narrow-m	*1.91*	*3*	*50*	*0.7*	*2.1*	*0.10*	*1*	*0*
A-narrow-s	*3.82*	*3*	*50*	*0.7*	*1.0*	*0.41*	*17*	*22*
A-wide	2.71	10	50	0.2	1.5	0.02	1	454
B-narrow[2]	2.71	3	100	0.7	0.7	0.82	203	12
B-narrow-w	*0.86*	*3*	*100*	*0.7*	*2.4*	*0.08*	*10*	*0*
B-narrow-m	*1.91*	*3*	*100*	*0.7*	*1.0*	*0.40*	*296*	*0*
B-narrow-s	*3.82*	*3*	*100*	*0.7*	*0.5*	*1.63*	*77*	*35*
B-wide	2.71	10	100	0.2	0.7	0.07	13	1341
C-narrow	2.71	3	200	0.7	0.4	0.37	389	17
C-narrow-w	*0.86*	*3*	*200*	*0.7*	*1.2*	*1.16*	*1*	*0*
C-narrow-m	*1.91*	*3*	*200*	*0.7*	*0.5*	*0.53*	*941*	*4*
C-narrow-s	*3.82*	*3*	*200*	*0.7*	*0.3*	*0.26*	*284*	*30*
C-wide	2.71	10	200	0.2	0.4	0.37	35	1658

[1]Based on incident flow of speed U = 0.2 m/s and a Coriolis parameter of $f = -1\times10^{-4}s^{-1}$

[2]Serves as control experiment

[3]Out of a total of 4000 particles released

2.3 Experimental design of numerical experiments

All experiments consider a continental slope that varies linearly between a depth of 1000 m at the offshore boundary and 100 m along a closed boundary over a distance of 40 km (**Figure 2a**). This corresponds to a bottom inclination of 900 m/40 km ≈ 0.025 (1.19° slope angle). The impact of variations of this slope on the results remains for future investigations. The region has a length of 50 km, resolved by an equidistant horizontal grid spacing of $\Delta x = \Delta y = 1$ km. A single submarine channel/canyon is embedded in the continental slope. Its axis runs perpendicular to the ambient isobaths. The channel vanishes in both shallower and deeper water. A variety of channel geometries are considered in a range of experiments (**Figure 2b**, **Table 1**) with channel depths H ranging between 50 and 200 m and channel widths W ranging between 3 and 10 km. A total of 60 vertical sigma levels are used, keeping the lowermost 5 adjacent levels at a maximum distance of 10 m to ensure a sufficient representation of the bottom Ekman layer in deeper portions of the model domain. The shallow boundary is treated as a nonpermeable coast. Zero-gradient conditions are used at the open lateral boundaries. The sea level along offshore boundary is kept at its initial value to facilitate the creation of long-slope geostrophic flows.

In all experiments the initial salinity field is horizontally uniform but varies linearly with depth. The vertical salinity increase is varied between 0.1, 0.5, 1 and 2 per 1000 m depth in subsequent experiments. This corresponds to values of the stability frequency N between 0.86×10^{-3} and 3.82×10^{-3} s^{-1} (between 3 and 13 cycles per hour) and captures natural value ranges found in the oceans. Note that N is defined by $N^2 = -g/\rho_o\, \partial\rho/\partial z$, where g = 9.81 m/$s^2$ is acceleration due to gravity and z is the vertical coordinate.

Each experiment is forced by the prescription of an along-slope barotropic pressure-gradient in the first 10 grid cells adjacent to the left boundary. This forcing, associated with a

virtual sea-level gradient of 0.1 mm per km, gradually creates a surface pressure field driving an along-slope geostrophic flow of $U \approx 0.2$ m/s in speed. To keep this speed relatively steady, the forcing magnitude is reduced when flow exceeds a speed of 0.2 m/s near the left boundary. For simplicity, variations of U are not considered in this study. Note that this flow is directed opposite to the propagation direction of free topographic Rossby waves (that have shallower water on their left in the southern hemisphere). This situation leads to the formation of standing topographic Rossby waves that are instrumental in cross-shelf fluxes induced by shelf-break canyons (see Kämpf, 2012; 2018).

After an initial adjustment phase of two days, a total of 4000 non-buoyant Lagrangian particles are gradually released upstream from the lower portion of the submarine channel within a random distance of up to 20 m from the seafloor (see Figure 2a). Particles are hereby released at a random horizontal location along the red line shown in Figure 2a at a rate of 33 particles per hour over a time interval of 5 days. Total water depth along the deployment line varies between 680 and 910 m. The total simulation times of experiments is 10 days, using external and internal numerical time steps of 3 s and 60 s, respectively. Particles reaching water depths <500 m by the end of the simulation are defined as "upwelled" particles. Particles staying within a distance of 5 km from the channel axis by the end of the simulation are defined as "trapped" particles.

Table 2: Configuration of additional experiments with numbers of upwelled and trapped particles

Experiment	Description	Σupwelled[2]	Σtrapped[2]
B-settling-1[1]	Particle settling speed $w_s = 0.1$ mm/s	347	49
B-settling-2[1]	Particle settling speed $w_s = 0.5$ mm/s	1694	508
B-settling-3[1]	Particle settling speed $w_s = 1$ mm/s	3012	2733
B-settling-4[1]	Particle settling speed $w_s = 5$ mm/s	3441	3924
B-reverse[1]	Bathymetry and forcing reversed in *x*-direction	0	0

[1]Has otherwise the same configuration as Experiment B-narrow (see Table 1)

[2]Out of the total of 4000 particles released

For completeness, Table 1 lists characteristic nondimensional numbers based on the geometric scales of the submarine channel/canyon. Based on canyon width W, the canyon Rossby number, $\mathrm{Ro} = U/(fW)$, measures the significance of inertial relative to rotational effects on the time scale $t^* = W/U$ is takes for a fluid parcel to surpass the channel. Here Ro varies between 0.2 for the wider canyons configurations and 0.7 for the narrower channels. We can also formulate a canyon Froude number, $\mathrm{Fr} = U/(NH)$, based on canyon depth H. The Froude number is a measure of the importance of stratification (Cushman-Roisin and Beckers, 2011). While this number is well defined in terms of hydraulic jump theory for flows over obstacles like mountains/sills, its meaning is less clear in the context of topographic depressions such as submarine channels. Fr ranges here between 0.3 and 4.7. The squared ratio $\mathrm{Bu} = (\mathrm{Ro}/\mathrm{Fr})^2$, known as Burger number, measures the relative abilities of stratification or rotation to limit vertical motion in geophysical fluids. In the experiments presented here, Bu varies between low values of 0.02 and maximum values of 1.63.

In addition to the experiments described in Table 1, the control experiment ("B-narrow") is repeated with the consideration of negatively buoyant particles of a constant vertical settling speed (**Table 2**). The settling speed is varied between 0.1 and 5 mm/s, noting that field

observations along the west Antarctica Peninsula revealed average settling speeds in the range of 0.12 – 1.7 mm/s (10 to 150 m per day) for marine particles ranging from equivalent spherical diameters of 70 mm to 6 mm (McDonnell and Buesseler, 2010). Deposition is not accounted for here under the assumption that there is always enough turbulence in the bottom-boundary layer to keep the particles in suspension. Moreover, for a complete understanding of the channel/flow interaction that enables the particle-upwelling mechanism, the control experiment ("B-narrow") is repeated with a horizontally reversed bathymetry (the channel is now located closer to the left boundary) and a reversal of the sign of the forcing. This creates an ambient geostrophic flow running into the propagation direction of free topographic Rossby waves. Again, 4000 Lagrangian particles are released upstream from the channel.

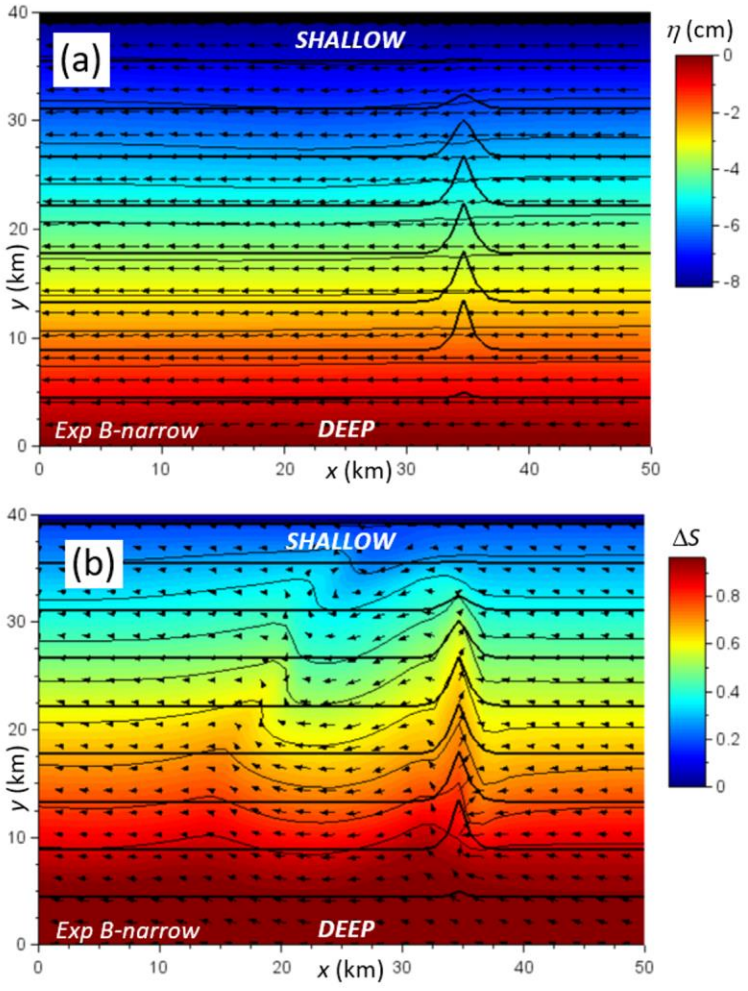

Figure 3: Experiment "B-narrow". Steady-state horizontal distributions after 5 days of simulation of a) sea-surface elevation η (colors and thin contours, cm) and b) near-bottom salinity anomalies relative to a constant value of 34 (color shading and thin contours, no units). Thick lines are bathymetric contours (arbitrary CI). Arrows illustrate the structure of horizontal currents.

206 **3 Results and Discussion**

207 3.1 Non-buoyant particles

208 First let us inspect the predictions of the control experiment "B-narrow". The applied
209 forcing creates a horizontal flow that crosses the submarine channel right-bounded by shallower
210 water and opposite to the propagation direction of free topographic Rossby waves (**Figure 3**).
211 Surface geostrophic are largely unidirectional and at a speed of ~0.2 m/s (Figure 3a). The
212 onshore sea-level gradient driving this flow is of the order of 1 cm per 5 km. Near the seafloor,
213 flow-bathymetry interactions have created a stationary topographic Rossby wave of a horizontal
214 wavelength of 12-15 km (Figure 3b). Note that such waves are the consequence of failure of
215 topographic steering, discussed by Kämpf (2018), that only develops if the ambient flow is
216 opposite to Rossby-wave propagation. Associated with this wave are alternating zones of
217 onshore and offshore flow with speeds of up to 0.2 m/s (**Figure 4**).

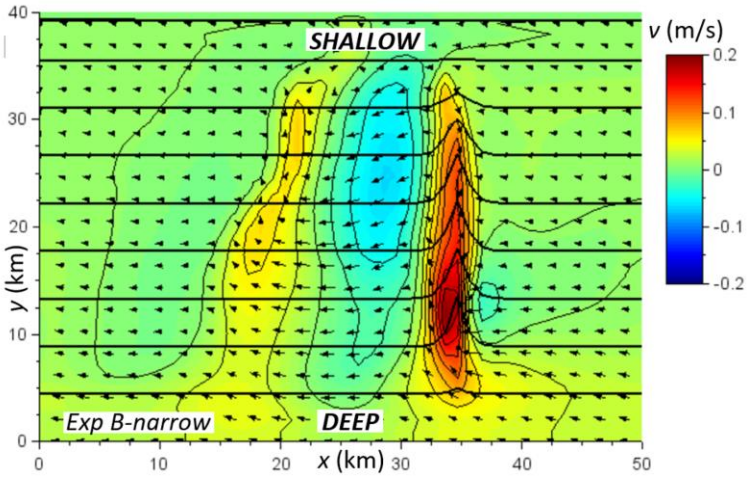

218

219 **Figure 4:** Experiment "B-narrow". Steady-state horizontal near-bottom distributions of the
220 cross-slope component (v) of velocity (color shading and thin contours, m/s) after 5 days of
221 simulation. The thick lines show bathymetric contours (arbitrary CI). Near-bottom refers to the
222 bottom-nearest model layer.

223 More importantly, the channel axis coincides with a persistent zone of up-channel
224 currents (which is the origin of Rossby-wave generation) that continue to exist for the entire
225 simulation (Figure 4). Initially flow disturbances associated with Rossby-wave formation lead to
226 a deformation of the near-bottom density field (See Figure 3b), but only until a steady-state
227 density distribution has established. To this end, the up-channel flow continues to exist despite
228 the creation of a steady-state situation. This implies that its advective effects on the density field
229 are counterbalanced by diffusive effects.

230 Rossby-wave disturbances remain confined to a zone of 100-150 m in vertical extent near
231 the seafloor (**Figure 5**). Hence, the up-channel flow within the submarine channel induces
232 enhanced turbulent diffusion in the vertical that effectively overrides the advective salinity
233 change. This can be tested with the simple advective-diffusive balance than can be written as:

234 $$v\,\partial S/\partial y = D_z\,\partial^2 S/\partial z^2 \qquad (3)$$

235 Using the scales $v \approx 0.2$ m/s and $\partial S/\partial y \approx -0.1/10$ km gives an estimate of the advective salinity
236 flux of -2×10^{-6} s^{-1}. On the other hand, simulated vertical profiles of salinity give an estimate of
237 the magnitude of $\partial^2 S/\partial y^2$ between -0.01 and -0.1 m^{-2} within the lower 50 m of the water column.
238 This implies that vertical diffusivities D_z in a range of 2×10^{-4} and 2×10^{-3} m^2/s are sufficient to
239 maintain a steady state, which is consistent with the predicted values (not shown).

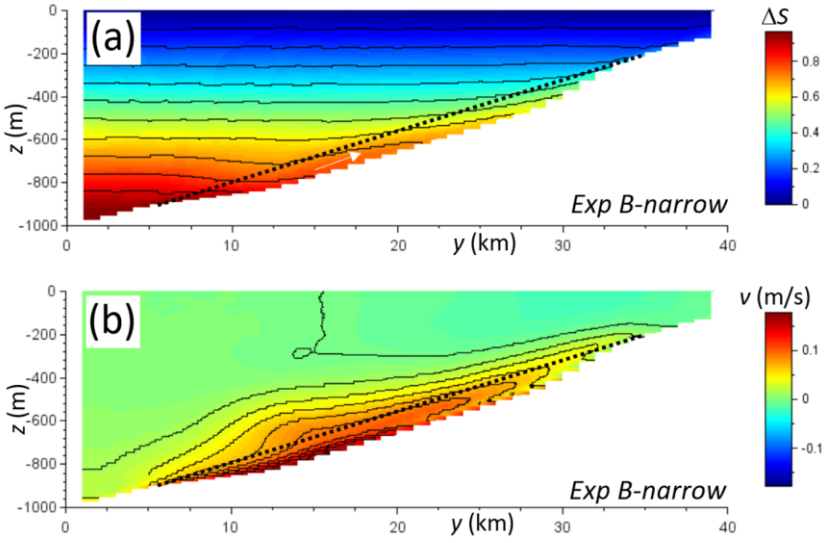

240

241 **Figure 5:** Experiment "B-narrow". Vertical transect at x = 35 km (along the channel axis) after 5
242 days of simulation of a) salinity anomaly (relative to a constant value of 34; color shading and
243 contours), and b) upslope velocity component (m/s; color shading and contours). The dotted line
244 indicates the shape of the ambient seafloor. In this display, the salinity and velocity field in σ
245 coordinates were mapped onto a Cartesian coordinate system with a vertical grid spacing of 1 m.

246 Non-buoyant Lagrangian particles follow largely the advective pathways of the flow.
247 Hence, the submarine channel provides a localized upslope pathway for particles that enter or
248 become entrained into the channel. Note that particles floating at distances >100 m from the
249 seafloor would transverse the channel without significant upwelling features. As this point it
250 should not be surprise for the reader to see that the submarine channel triggers a general upward
251 deflection of particles that become entrained by the near-bottom flow (**Figure 6**). To this end,
252 particles become generally dispersed in the upslope direction (Figure 6a) whereby particles that
253 escape the influence of the up-channel flow (e.g. via turbulent velocity fluctuation) are rapidly
254 moved away from the channel by the ambient along-slope current. Particles remaining inside the
255 channel form a concentrated stream the exit the channel near its head (Figure 6b). In this
256 experiment, 213 particles are upwelled to total water depths <500 m. The head of the submarine
257 channel serves as a bottleneck; that is, it becomes a focus region of particles that are imported by
258 the ambient along-slope flow from a variety of total water depths. It should be noted only 6
259 particles (not shown) are still located in vicinity of the channel by the end of the simulation.

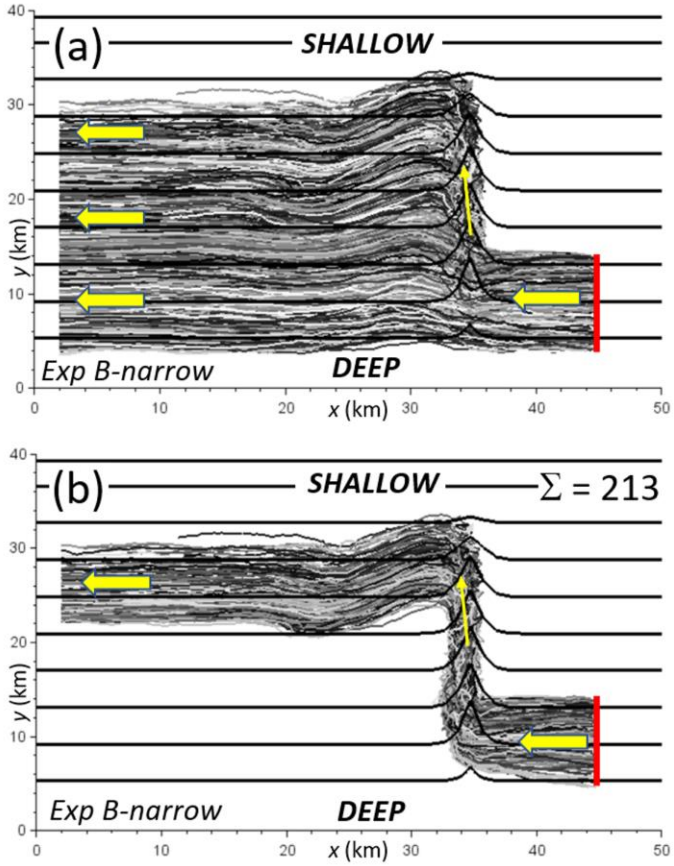

Figure 6: Experiment "B-narrow". Trajectories of a) all (4000) Lagrangian particles used in the simulation, and b) a subset of 214 particles that become upwelled to total water depths <500 m by the end of the simulation. The yellow arrows indicate flow directions. Red lines denote the release location of particles.

The degree of vertical salinity (density) stratification influences the particle upwelling processes. In Experiment B-narrow, a slight reduction of the stability frequency from $N = 2.71\times10^{-3}$ s^{-1} to 1.91×10^{-3} s^{-1} leads to a 46% increase in the number of upwelled particles to 293. In contrast, both a stronger ($N = 3.82\times10^{-3}$ s^{-1}) and weaker stratification ($N = 0.86\times10^{-3}$ s^{-1}) markedly reduce the number of upwelled particles to 77 and 10, respectively (see Table 1). This suggests that some but not too much static stability is required to maximize the particle-upwelling flux. Note that the strongest particle-upwelling flux in this experiment series is characterized by a canyon Burger number of Bu ≈ 0.4.

The degree of vertical density stratification influences the evolution and wavelength of the resultant internal topographic Rossby wave. In the case of weak density stratification ($N = 0.86\times10^{-3}$ s^{-1}) the internal Rossby wave fails to develop. In the other cases, the wavelength approximately follows the relationship $\lambda \sim 1/N^2$, noting that the case of strong density stratification ($N = 3.82\times10^{-3}$ s^{-1}) yields a wavelength of 10 km. It should be noted that only few particles become trapped in the presence of a narrow submarine channel characterized by a relatively large canyon Rossby number ≈ 0.7. This situation substantially changes for wider submarine canyons, as discussed in the following.

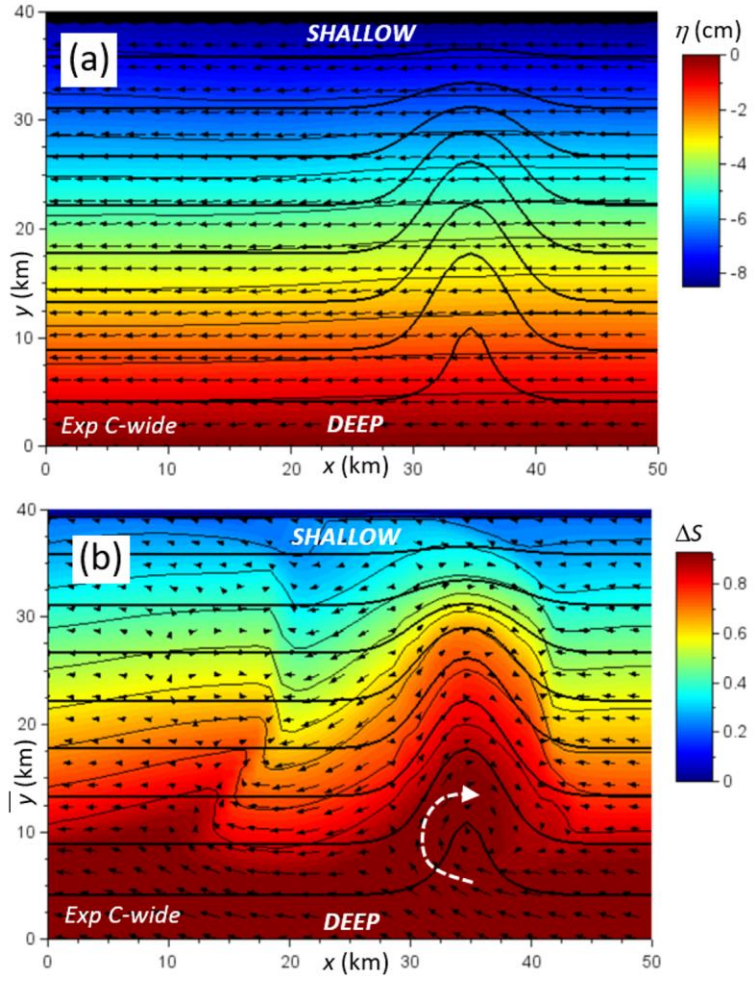

Figure 7: Same as Figure 3, but for experiment ”C-wide”**.** The curved arrow in panel b) indicate the creation of a mesoscale eddy in lower portions of the canyon.

In the presence of a wider submarine canyon in experiment C-wide, the interaction between the incident flow with the seafloor depression creates a standing topographic Rossby wave (**Figure 7**). This wave only develops in a near-bottom layer (Figure 7b) without any noticeable surface expression (Figure 7a). Again, the canyon-flow interaction leads to the development of a zone of up-canyon flows (**Figure 8**). In contrast to the narrow channel (see Figure 4), the upslope velocity component becomes weaker in upper portion of the canyon. Due to increased canyon width, however, this zone of up-canyon flows is accompanied by an adjacent zone of enhanced downcanyon flows.

This flow field, characterized by a reduced canyon Rossby number of Ro ≈ 0.3, limits particles to primarily enter the canyon via its mouth from where there recirculate inside the canyon while slowly moving upward on the continental slope (**Figure 9**). Kämpf (2006) described similar eddy-type features in the lower portions of submarine canyons that tend to disappear for higher flow speeds (i.e. higher canyon Rossby numbers). In this case, the

submarine canyon operates more as a trap of nonbuoyant particles, noting that a total of 1658 particles are still near the canyon by the end of the simulation. High rates of particle trapping are seen in all experiments of low canyon Rossby numbers (see Table 1).

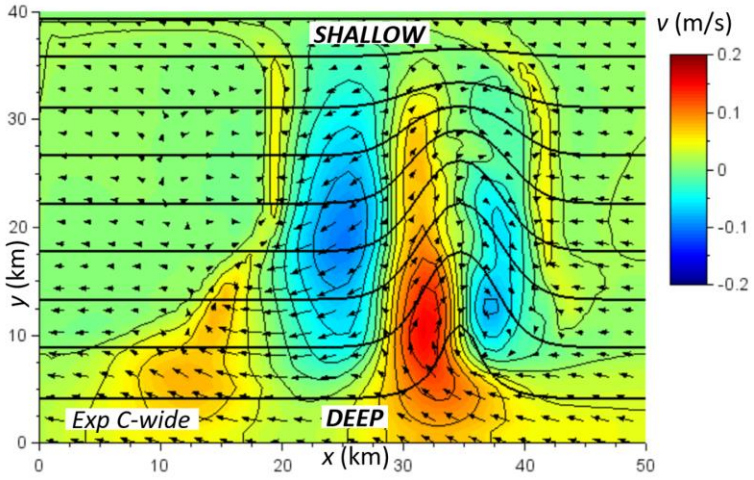

Figure 8: Same as Figure 4, but for experiment "C-wide"**.**

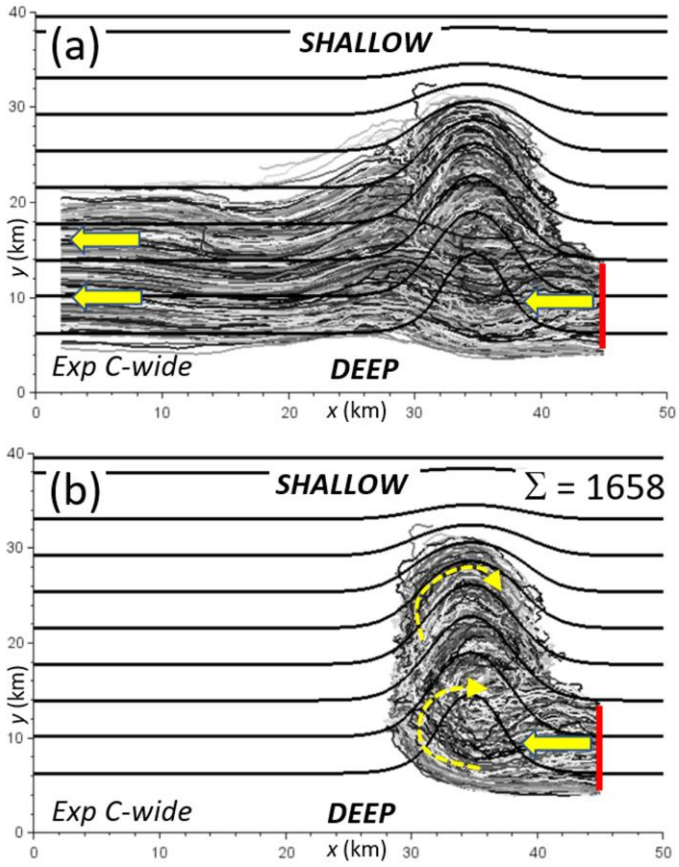

Figure 9: Experiment "C-wide"**.** Trajectories of a) all (4000) Lagrangian particles used in the simulation, and b) subset of 1658 particles that are still located near the canyon by the end of the

simulation. The yellow arrows indicate flow directions. Red lines denote the release location of particles.

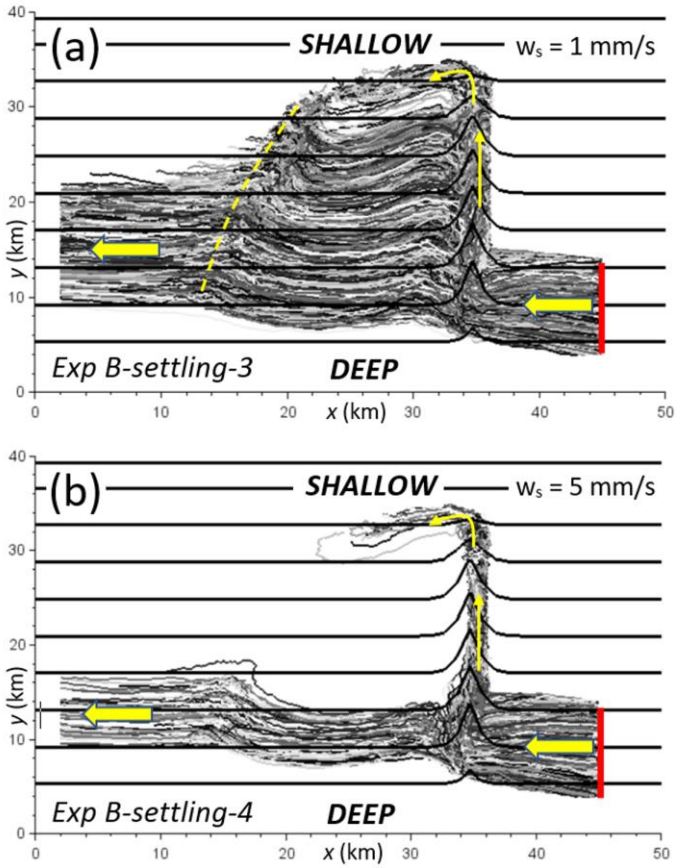

Figure 10: Same as Figure 9a, but for a) experiment "B-settling-3" and b) experiment "B-settling-4" (see Table 2). The dashed line in panel a) coincides with the first wave crest of the topographic Rossby wave (see Figure 3b).

3.2 Negatively-buoyant particles

Gravitational settling of negatively-buoyant particles significantly increases the up-channel particle flux (see Table 2, **Figure 10**). For instance, a settling speed of w_s = 1 mm/s leads to the upwelling of ~68% of all particles released past the 500-m isobath. In this case, there also appears some modification of the pathway of particles along the first first wave crest of the topographic Rossby wave. The upwelling efficiency increases to 98% for a high settling speed of w_s = 5 mm/s. In this case, almost all particles are channeled upward on the continental slope exiting the submarine channel through its head in shallower water (see **Figure 10b**). This interesting and at first sight perplexing feature can be explained by the fact that negatively-buoyant particles tend to sink while crossing the submarine channel. On the time scale of channel crossing, $W/U \approx 3$ km/0.2 m/s ≈ 4.17 hours, a particle of w_s = 1 mm/s can sink a vertical distance of 15 m. Due to this effect, it becomes clear that there is an increased chance that larger particles become entrained into the up-channel flow. Due to gravitational settling, particles can enter the submarine channel at any location on the continental slope (provided they are located sufficiently

close to the seafloor). Larger-size particles of increased settling speed exit the channel's head in a concentrated stream. Hence, the channel's head is an optimum location for marine species feeding on such larger-size organic particulate matter.

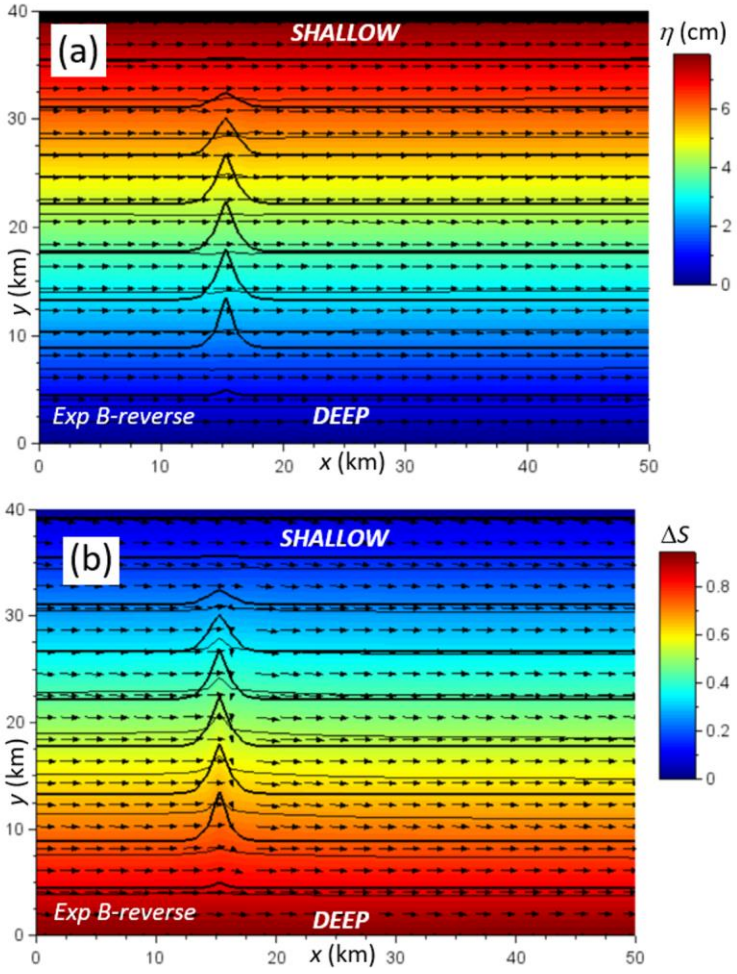

Figure 11: Same as Figure 3, but for experiment "B-reverse"**.**

3.3 Reversing the ambient flow direction

An ambient along-slope current that is left-bounded by shallower water runs parallel to the propagation direction of topographic Rossby waves in the southern hemisphere. Such a current cannot operate to hold a Rossby wave in place. Hence, significant flow disturbances do not develop in the case and the flow is smoothly topographically steered along isobaths (Kämpf, 2012; 2018), as seen in the predictions (**Figure 11**). While some cross-slope velocity anomalies develop in vicinity of the submarine channel **(Figure 12**), these anomalies fail to create a persistent particle upwelling (**Figure 13a**, compare with **Figure 13b**). For completeness, it should be noted that the inclusion of particle settling does have much of an effect here. Overall, the findings presented here suggest that only along-slope flows that are right-bounded by shallower water can operate as an agent of concentrated up-channel flows of particulate matter on continental slopes.

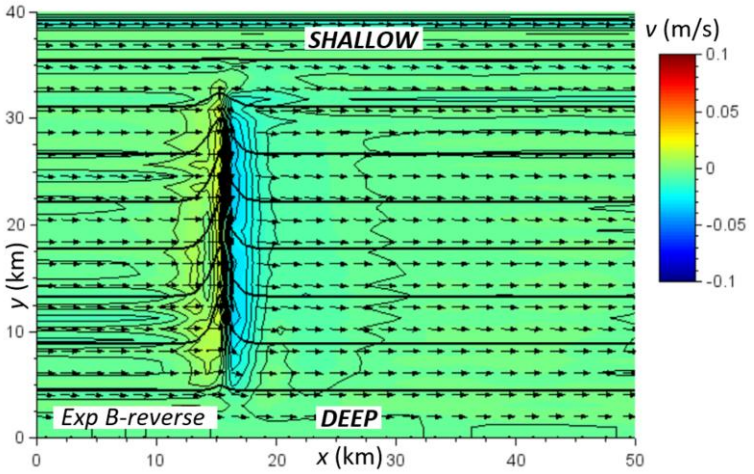

Figure 12: Same as Figure 4, but for experiment "B-reverse"**.**

4 Conclusions

This work conclusively demonstrates that there exist physical processes that can return sinking particles of organic matter across density surfaces into shallower water on continental slopes. This feature is made possible by the interaction of an along-slope flow in interaction with a submarine channel, which creates a narrow bottom-parallel up-channel flow inside submarine channels. On a timescale of a few days, while no longer modifying the density field, this flow can maintain a continuous up-channel stream of particles, which is consistent with the conceptual model (see Figure 1) underpinning this work. The cross-channel geometry provides a trapping mechanism for settling particles, while the up-channel flow is the agent of particle transportation. This current also appears sufficiently strong to prevent the deposition of particles (not accounted for in this study).

Findings of this study have identified a physical mechanism that creates spatial concentrations of particulate matter in submarine channels. Wider submarine canyons (characterized by a canyon Rossby number < 0.5) supports the creation of a return circulation near their mouth that operates to trap particles at greater water depths. The upslope flow of particles is more pronounced for narrow submarine channels (characterized by a canyon Rossby number > 0.5). This feature of upward channeling of both non-buoyant and negatively buoyant particles is the first concrete clue that could explain why the head regions of some submarine canyons/channels are sources of particulate matter for suspension feeders whereas others are not. The author believes that the upwelling of particulate matter on continental slopes plays a central role in marine nutrient cycles and marine food webs relying on suspension feeding.

Future studies should explore the particle transportation mechanism in more realistic settings. For instance, the Bremer Canyon group in the western Great Australian Bight serves as a seasonal feeding hotspot for the largest annual aggregation of orcas (Orcinus orca) in the southern hemisphere. Each year in austral summer >100 individuals come to feed in a region that has total water depths of 800-1000 m (Bouchet et al., 2018). The specific reasons for this natural wonder are still a mystery. Could it be that spatial concentrations of organic particles matter at depths are the trigger of this specific marine food web?

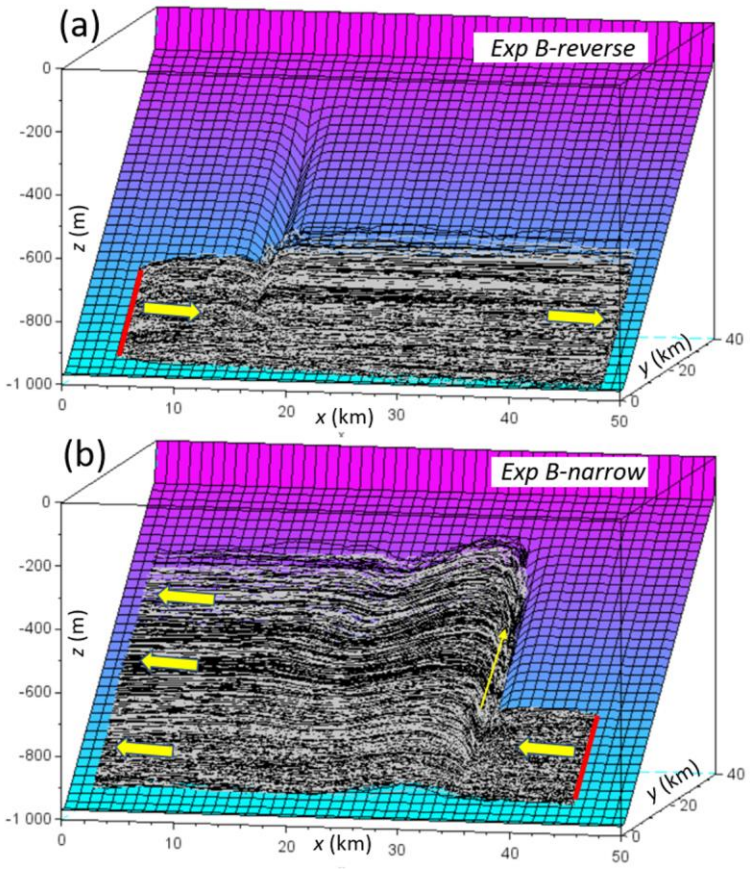

Figure 13: Three-dimensional visualization of the trajectories of 4000 non-buoyant particles in the experiments a) "B-reverse" and b) "B-narrow". Yellow arrows indicate flow direction. Red lines indicate the release location of particles.

Acknowledgments

The author is grateful to Matthias Tomczak, who sadly passed away in May 2019, for discussions on early versions of this research. The author has no real or perceived financial conflicts of interests of any kind. This work uses the original version of the COHERENS model (Luyten et al.,1999). The FORTRAN code with the configuration of experiment "B-narrow" and instructions are available from doi.org/10.5281/zenodo.3747013. Simulation data for this experiment can be downloaded at doi.org/10.5281/zenodo.3747057. Included are also Scilab scripts for the visualization of data. This research has not received external research funding.

References

Ådlandsvik, B., Bartsch, J., Brickman, D., et al. (2009), Manual of Recommended Practices for Modelling Physical – Biological Interactions During Fish Early Life. *Technical Report*. IFREMER, Dépt., EMH BP 21105 FR-44311 Nantes, Cedex 03, France. https://archimer.ifremer.fr/doc/00157/26792/, last accessed 9/4/20.

Bouchet, P. J., Meeuwig, J. J., Erbe, C., Salgado-Kent, C.P., Wellard, R., & Pattiaratchi, C.B. (2018), Bremer Canyon Emerging Priorities Project EP2: *Final Report*. National Environmental Science Programme, Marine Biodiversity Hub. University of Western Australia, 32 p., https://research-repository.uwa.edu.au/en/publications/bremer-canyon-emerging-priorities-project-ep2-final-report-occurr, last accessed 10/4/20.

Collier, R. W., & Lilley, M. D. (2005), Composition of shelf methane seeps on the Cascadia Continental Margin, *Geophysical Research Letters*, 32, L06609, doi:10.1029/2004GL022050.

Cushman-Roisin, B., & Beckers, J.-M. (2011), *Introduction to Geophysical Fluid Dynamics: Physical and Numerical Aspects*, Second Edition, International Geophysics Series, vol. 101, Elsevier/Academic Press.

Delhez, E. J. M., Campin, J. M., Hirst, A. C., & Deleersnijder, E. (1999), Toward a general theory of the age in ocean modelling. *Ocean Modelling*, 1, 17–27.

Einstein, A. (1905), Über die von der molekularkinetischen Theorie der Wärme geforderte Bewegung von in ruhenden Flüssigkeiten suspendierten Teilchen. *Annalen der Physik* (in German), 322 (8), 549–560. doi:10.1002/andp.19053220806.

Hentschel, B., & Shimeta, J. (2008), Suspension feeders. In: Jorgensen, S. (ed), *Encyclopedia of Ecology*. Elsevier, Amsterdam, pp 3437–3442.

Kämpf, J. (2006), Transient wind-driven upwelling in a submarine canyon: a process-oriented modelling study. *Journal of Geophysical Research*, 111, C11011, doi:10.1029/2006JC003497

Kämpf, J., Payne, N., & Malthouse, P. (2010), *Marine connectivity in a large inverse estuary*, *Journal of Coastal Research*, 26 (6), 1047–1056. doi:10.2112/JCOASTRES-D-10-00043.1.

Kämpf, J. (2012), Lee effects of localized upwelling in a shelf-break canyon. *Continental Shelf Research*, 42, 78–88. doi:10.1016/j.csr.2012.05.005.

Kämpf, J., & Chapman, P. (2016), *Upwelling Systems of the World: A Scientific Journey to the Most Productive Marine Ecosystems*, pp. 433, Springer International Publ., Switzerland.

Kämpf., J., (2018), On the dynamics of canyon–flow interactions. *Journal of Marine Science and Engineering*, 6(4), 129. doi:10.3390/jmse6040129.

Levin, L. A., Mendoza, G. F., Grupe, B. M., et al. (2015), Biodiversity on the Rocks: Macrofauna Inhabiting Authigenic Carbonate at Costa Rica Methane Seeps. *PLoS One*, 10(7):e0131080. doi:10.1371/journal.pone.0131080.

Liu, G., Bracco, A., & Passow, U. (2018), The influence of mesoscale and submesoscale circulation on sinking particles in the northern Gulf of Mexico. *Elementa: Science of the Anthropocene*, 6(1), p.36, doi.org/10.1525/elementa.292.

Luyten, P. J., Jones, J. E., Proctor, R., Tabor, A., Tett, P., & Wild-Allen, K. (1999), COHERENS - A Coupled Hydrodynamical-Ecological Model for Regional and Shelf Seas: User Documentation; MUMM Report; Management Unit of the North Sea: Brussels, Belgium, 914p.

Maier-Reimer, E., (1980), On the formation of salt water wedges in estuaries. *Lecture Noteson Coastal and Estuarine Studies*, 1, 91–101.

McDonnell, A. M. P.**,** Buesseler, K. O**. (**2010), Variability in the average sinking velocity of marine particles. *Limnology and Oceanography*, 55, 2085–96. doi:10.4319/lo.2010.55.5.2085.

Mullineaux, L. S., Metaxas, A., Beaulieu, S. E., Bright, M., Gollner, S., Grupe, B. M., & Won, Y.-J. (2018), Exploring the ecology of deep-sea hydrothermal vents in a metacommunity framework. *Frontiers in Marine Science*, 5 (49), 1–27, doi:10.3389/fmars.2018.00049.

Oey, L.-Y., Mellor, G. L., & Hires, R. I. (1985), A three-dimensional simulation of the Hudson-Raritan estuary. Parts I, II and III. *Journal of Physical Oceanography*, 15, 1676–1720. doi:10.1175/1520-0485(1985)015<1693:ATDSOT>2.0.CO;2.

Sandery, P. A., and Kämpf, J. (2007), Transport timescales for identifying seasonal variation in Bass Strait, south-eastern Australia. *Estuarine, Coastal and Shelf Science*, 74 (4), 684–696, doi:10.1016/j.ecss.2007.05.011.

Santora, J. A., Zeno, R., Dorman, J. G., & Sydeman, W. J. (2018), Submarine canyons represent an essential habitat network for krill hotspots in a large marine ecosystem. *Scientific Reports*, 8:7579. doi:10.1038/s41598-018-25742-9.

Siegel, D. A., Granata, T. C., Michaels, A. F., and Dickey, T. D. (1990), Mesoscale eddy diffusion, particle sinking, and the interpretation of sediment trap data, *Journal of Geophysical Research*, 95(C4), 5305–5311, doi:10.1029/JC095iC04p05305.

Stokes, G. G. (1851), On the effect of internal friction of fluids on the motion of pendulums, *Transactions of the Cambridge Philosophical Society*, 9, part II: 8–106.

Taylor, G. I. (1922) Diffusion by continuous movements. *Proceedings of London Mathematical Society*, 2, 196–212.

van Sebille, E., Griffies, S. M., Abernatheyd, R., et al. (2018), Lagrangian ocean analysis: Fundamentals and practices. *Ocean Modelling*, 121, 49–75. doi: 10.1016/j.ocemod.2017.11.008.

Yu, Q., Wang, Y., Gao, J., Gao, S., & Flemming, B. (2014), Turbidity maximum formation in a well-mixed macrotidal estuary: The role of tidal pumping, *Journal of Geophysical Research-Oceans*, 119, 7705–7724, doi:10.1002/ 2014JC010228.